Electronic Supplementary Information (ESI)
for
Binding Site Exchange Kinetics revealed through Efficient Spin-Spin Dephasing of Hyperpolarized ^{129}Xe

Martin Kunth and Leif Schröder

October 12, 2020

Contents

S1 Special Carr-Purcell-Meiboom-Gill Conditions in the Case of Reversibly Bound Xe

S1.1 General Aspects and Sensitivity Considerations

Systems investigated with hyperpolarized, caged ^{129}Xe are often characterized by a large chemical shift difference, $\Delta\omega \approx 10^3 \ldots 10^4$ Hz, between the pool of free Xe (pool A) and bound Xe (pool B). The solubility of Xe yields noble gas concentrations in Xe-saturated solutions that can reach mM values. However, the solubility of Xe hosts is often much lower and together with the fact that only a certain fraction of the binding sites is occupied with Xe, the fraction of the B pool f_{B} is less than 1 % in such systems. Whereas this imposes challenging conditions for direct detection, this allows a significant simplification for the treatment of the effective spin-spin relaxation rate, $R_{2,\mathrm{eff}}$, in the detected bulk pool.

We demonstrate that for ^{129}Xe with its large chemical shift range the evolution can be strongly dominated by the jumps in Larmor frequency and that the Carr-Purcell-Meiboom-Gill (CPMG) experiment represents special conditions which simplify the commonly used Carver-Richards solution significantly. In fact, eventually it does not matter if the phase coherence between spins that transfers from pool B into the detected pool A is lost in B because of “classic” spin-spin relaxation or because of stochastic spin-spin dephasing due to a large chemical shift jump.

Xe systems with an interaction partner or host spin pool provide various conditions to study the effective spin-spin relaxation rate, $R_{2,\mathrm{eff}}$. Independent from CPMG measurements, parameters of the exchange-connected spin pools can be determined by quantitative chemical exchange saturation transfer with hyperpolarized Xe (Hyper-CEST) analysis[1] based on the full Hyper-CEST (FHC) solution[2]; whereas CPMG measurements observe the combined loss of phase coherence from $R_{2,\mathrm{eff}}$ in spin pool B and from frequency jumps between the spin pools, the chemical exchange saturation transfer (CEST) effect represents an actively induced fast perturbation in spin pool B that allows to isolate the exchange rate and to estimate an upper limit of the spin-spin relaxation rate in absence of any exchanging site, $R_{2,0}$.

In general, analysis of both the Hyper-CEST effect and the exchange-induced relaxation can be seen in the context of the intrinsic, classic spin-spin relaxation rate in each of the two spin pools individually, $R_{2,\mathrm{A}}$ and $R_{2,\mathrm{B}}$. Since in the relaxometry experiment in Figure 3a in the manuscript, $R_{2,\mathrm{eff}}$ approaches $R_{2,\mathrm{A}}$ for zero host concentration (***i.e.***, [host] = 0 μM), we observe a function of the type $f(x) = m \cdot x + y_0$ with y_0 denoting the y-intercept corresponding to $R_{2,0}$. We thus denote from here on and throughout both the manuscript and this ESI $R_{2,0} = R_{2,\mathrm{A}}$. Whereas for the FHC solution it is critical that the exchange driven saturation transfer out of the CEST pool is dominant[1], $k_{\mathrm{BA}} \gg R_{2,\mathrm{B}}$, the relaxometry data is insensitive to the intrinsic $R_{2,\mathrm{B}}$ according to Millet ***et al.***[3] as long as $|R_{2,0} - R_{2,\mathrm{B}}| \ll \Delta\omega(f_{\mathrm{A}} - f_{\mathrm{B}})$; with $f_{\mathrm{A/B}}$ denoting the fractional size of spin pool A/B, respectively. The dominating $\Delta\omega$ of $\sim 10^4$ Hz allows a generous $R_{2,\mathrm{B}}$. Nonetheless, $R_{2,\mathrm{B}}$ is diffcult to measure. To validate that this inequality is true for Xe, consider the other extreme and suppose that $|R_{2,0} - R_{2,\mathrm{B}}| \sim \mathcal{O}(10^4)$ s^{-1}. Then, $T_{2,\mathrm{B}} = 1/R_{2,\mathrm{B}} \sim \mathcal{O}(10^{-4})$. Now consider a CEST experiment in which RF saturation pulses are applied typically for several seconds. If the $T_{2,\mathrm{B}}$ of bound Xe would be that short, then all magnetization must be gone long before the RF saturation pulse would impact. The fact that even weak saturation pulses of 1.1 μT (slow rotation of the magnetization with ω_1 = 12.9 Hz), induce a CEST effect under comparable sample conditions[1] means that the exchange must be dominant over intrinsic $R_{2,\mathrm{B}}$ relaxation. Therefore, $R_{2,\mathrm{B}}$ is at maximum in the order of $R_{2,0}$, greatly fulfilling Millet’s inequality above.

The detection of the bulk pool via $R_{2,\mathrm{eff}}$ is much more feasible than direct detection of the host pool at low concentrations.

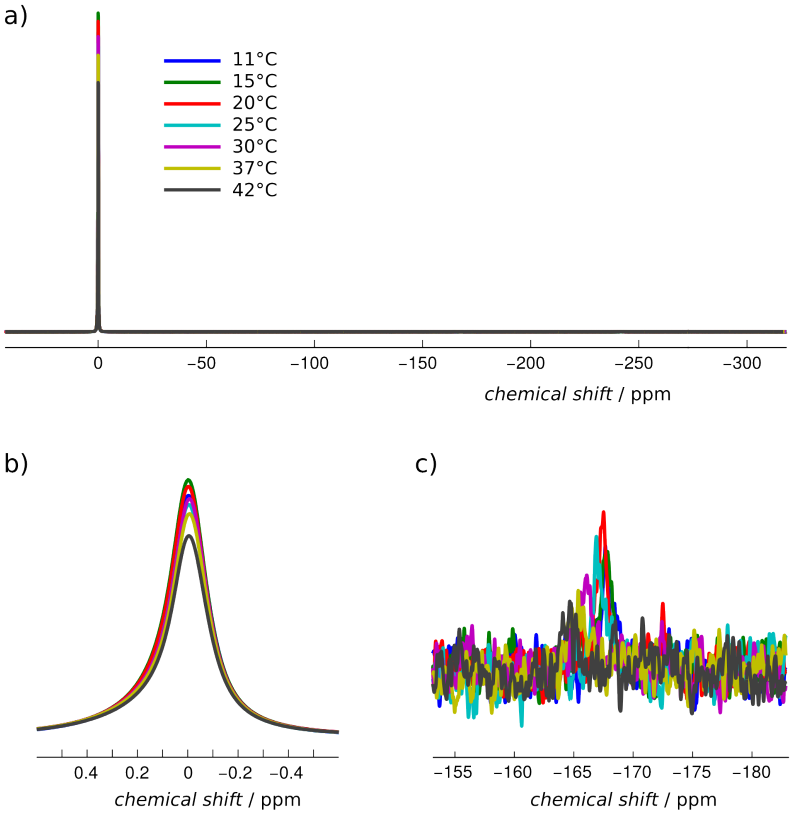

Figure S1: Direct ^{129}Xe-NMR spectroscopy of [CrA] = 100 μM in DMSO at different temperatures (intensity of each spectrum was scaled to the same noise level; chemical shift given relative to the resonance of free Xe in DMSO).

S1.2 Sensitivity Considerations

The host CrA-ma had been previously investigated in DMSO using the same SEOP setup and NMR equipment [1]. To study the off rate, k_{BA}, by line broadening at these small concentrations of material we are using ($f_{\mathrm{A}} \gg f_{\mathrm{B}}$) with direct Xe NMR spectroscopy, then 1) only the peak of bound Xe shows line boarding but is too small in signal intensity to obtain significant statistic without extensive averaging, and 2) the easy detectable signal of free xenon (at 0 ppm) is not line broaded by the exchange rate because of highly diluted material. The higher bulk pool signal is thus not suitable to quantify the exchange. This is illustrated in Figure S1. The line widths determined with the `peakw` command in `Topspin` ranged between 21.12 Hz (for 284 K) and 19.53 Hz (for 303 K) and thus did not show any significant dependence on the exchange rate that was controlled through the temperature.

The detection of the bulk pool via $R_{2,\text{eff}}$ is much more feasible than direct detection of the host pool at low concentrations. The following estimation illustrates that the detection limit for this system should be in the low μM range:

At 310 K, the fit result gave $R_{2,0}$ = (0.24 ± 0.04) s^{-1}. Hence, the change in $R_{2,\text{eff}}$ caused by the host should be at least 0.08 s^{-1}. Given a transverse relaxivity of 23.2 s^{-1} mM^{-1}, ca. 3.4 μM host needs to be present.

At 295 K, the fit result gave $R_{2,0}$ = (0.09 ± 0.01) s^{-1}. Hence, the change in $R_{2,\text{eff}}$ caused by the host should be at least 0.02 s^{-1}. Given a transverse relaxivity of 10.9 s^{-1} mM^{-1}, ca. 1.8 μM host needs to be present.

These concentrations are ca. 100-fold lower than the above-mentioned example with direct detection. Investigating the exchange effect with direct detection would then require $(100)^2 \cdot 64$ = 640 000 scans to obtain a reliable SNR and thus be beyond realistic experimental conditions.

S1.3 Exchange Parameter Nomenclature

Our work uses the exchange rates as in McConnell's Bloch-equation modification[4], but we preferred to use k, than τ as done by McConnell. Specifically, we use the equivalents: $k_{\text{AB}} \rightarrow 1/\tau_{\text{A}}$, and $k_{\text{BA}} \rightarrow 1/\tau_{\text{B}}$. Additionally, there is more exchange going on than dissociation from the cage. A degenerate Xe-CrA-ma exchange also occurs [5, 6] (for CrA-ma in water it was measured to be about 5,600 M^{-1} s^{-1} for Xe[6]). However, we estimated the contribution of degenerate Xe-CrA-ma exchange for our experimental condition in this study to be < 2 % out of ca. 300 s^{-1} for CrA-ma in DMSO (Our maximum Xe concentration was 2,340 μM at 295 K $\Rightarrow$ 2.34 10^{-3} M $\cdot$ 5600 M^{-1} s^{-1} = 13.104 s^{-1}; however, CrA-ma's occupancy for Xe in water is ca. 29 %[7, 8], whereas CrA-ma's occupancy for Xe in DMSO is ca. 6-9 %[1, 9, 7], *i.e.*, ca. 3.5-fold lower. This makes the degenerate Xe-CrA-ma exchange contribution accordingly less significant: 13.104 s^{-1}/3.5 = 3.7 s^{-1} which is by far smaller than our experimental precision in k_{BA}), and therefore, not included in the further treatment.

S1.4 Theoretical Considerations

The CPMG spin echo trains are typically analyzed with the Carver-Richards equation (Eq. 41 in [10])

$$R_{2,\text{eff}} \cong R_{2,0} + \frac{1}{2\tau} - \frac{1}{t_{\text{CP}}} \cdot \sinh^{-1} \mathcal{F} \tag{S1}$$

(with 2τ being the lifetime between exchanges; t_{CP} being the time between 180° RF pulses; and $\mathcal{F}$ being a function of the fractional populations of the sites, P_{a} and P_{b}; the relative chemical shift difference, $\Delta\omega$; t_{CP}; 2τ; thus: $\mathcal{F}(P_{\text{a}}, P_{\text{b}}, \Delta\omega, t_{\text{CP}}, 2\tau)$). This simplifies in the limit of large chemical shift differences $\Delta\omega$ (re-defining "slow" exchange) as done by Millet *et al.* [3] (Eq. 9 therein):

$$R_{2,\text{eff}} \cong R_{2,0} + f_{\text{B}} \cdot k_{\text{ex}} \tag{S2}$$

The question remains, how "leaky" 180° RF pulses in the CPMG experiment introduce $R_{2,\text{eff}}$ quantification-errors. Importantly, Baldwin has shown that such quantification-errors can accumulate seriously over the course of pulse repetition and suggests a correction term for that[11]. In the following, we show that this correction term vanishes for dominant $\Delta\omega$.

S1.4.1 Baldwin's Correction to the Carver-Richards Equation

In this section we will demonstrate that Baldwin's correction term disappears. The notation as used in Baldwins solution deviates slightly from the notation of spin pool A and spin pool B, and uses G and E for ground and exited state, respectively. Specifically, our notation relates to that used by Baldwin the following: $k_{\mathrm{GE}} \to k_{\mathrm{AB}}$; $k_{\mathrm{EG}} \to k_{\mathrm{BA}}$; $f_{\mathrm{A}} \to P_{\mathrm{G}}$; $f_{\mathrm{B}} \to P_{\mathrm{E}}$; $R_{2,\mathrm{A}} \to R_2^{\mathrm{G}}$, and $R_{2,\mathrm{B}} \to R_2^{\mathrm{E}}$.

The important point is that the argument in the $\ln()$ term in eq. (50) of Ref. [11] is close enough to 1. This is given for

$$\sqrt{\nu_{1\mathrm{C}}^2 - 1} \approx \nu_2 + 2 \cdot p_{\mathrm{D}} \cdot k_{\mathrm{AB}} \tag{S3}$$

using our notation of k_{AB} instead of k_{GE}. Here, $\nu_{1\mathrm{C}}$, ν_2, and p_{D} are functions of τ_{CP}, $\Delta\omega$, k_{AB}, k_{BA}, $R_{2,\mathrm{A}}$, and $R_{2,\mathrm{B}}$. This approximation is given for $p_{\mathrm{D}} \cdot k_{\mathrm{AB}} \to 0$ and happens according to Baldwin for $f_{\mathrm{B}} < 1$ %. In such cases, the large dominance of pool A causes $k_{\mathrm{AB}} \to 0$. Such $f_{\mathrm{B}} < 1$ % is easily achievable with hp Xe because small changes in the relaxation of the A pool can be detected and require only a minute concentration of pool B. But in our case it is not only the pool size ratio that helps to approach $p_{\mathrm{D}} \cdot k_{\mathrm{AB}} \to 0$ (we have $k_{\mathrm{AB}} \approx \mathcal{O}(10^{-1})$). The dominant $\Delta\omega$ once more has an impact and the parameter p_{D} that also becomes small. Its definition is given in Baldwin's Eq. 45

$$p_{\mathrm{D}}\, N = \nu_{1\mathrm{S}} + (F_1^a + F_1^b)\sinh(\tau_{\mathrm{CP}} E_1). \tag{S4}$$

The a and b indices of F_1 in Equation S4 were introduced by Baldwin and are different to our pool label notation of "A" and "B". With

$$\nu_{1\mathrm{S}} = F_0 \sinh(\tau_{\mathrm{CP}} E_0) - F_2 \sinh(\tau_{\mathrm{CP}} E_2) \tag{S5}$$

we determine the parameters for the amplitudes and arguments of these hyperbolic functions. To do so, Baldwin defines four quantities, $h_1, \ldots, h_4$, in Eq.s (12-13) that yield the (complex) eigenvalues f_{00} and f_{11} (which themselves represent two characteristic frequencies of the ground state and excited state). The first two relevant terms of these can be approximated as follows:

$$h_1 = 2\,\Delta\omega\,(R_{2,\mathrm{B}} - R_{2,0} + k_{\mathrm{BA}} - k_{\mathrm{AB}}) \approx 2\,\Delta\omega\,(R_{2,\mathrm{B}} - R_{2,\mathrm{A}} + k_{\mathrm{BA}}) \approx \mathcal{O}(10^4\, 10^2) = \mathcal{O}(10^6) \tag{S6}$$

$$h_2 = (R_{2,\mathrm{B}} - R_{2,0} + k_{\mathrm{BA}} - k_{\mathrm{AB}})^2 + 4\, k_{\mathrm{BA}}\, k_{\mathrm{AB}} - \Delta\omega^2 \tag{S7}$$

$$\approx (R_{2,\mathrm{B}} - R_{2,0} + k_{\mathrm{BA}})^2 + 4\, k_{\mathrm{BA}}\, k_{\mathrm{AB}} - \Delta\omega^2 \approx -\Delta\omega^2 \approx \mathcal{O}(10^8) \tag{S8}$$

Because $\Delta\omega^2$ is by far the dominant term, these terms simplify significantly, even when compared to the exchange rates. h_1 and h_2 are then used in the following two parameters:

$$h_3 = \frac{1}{\sqrt{2}}\sqrt{+h_2 + \sqrt{h_1^2 + h_2^2}} \approx \frac{1}{\sqrt{2}}\sqrt{-\Delta\omega^2 + \sqrt{4\,\Delta\omega^2 (R_{2,\mathrm{B}} - R_{2,0} + k_{\mathrm{BA}})^2 + \Delta\omega^4}} \tag{S9}$$

$$\approx \frac{1}{\sqrt{2}}\sqrt{-\Delta\omega^2 + \Delta\omega^2} = 0 \tag{S10}$$

because the contribution from $h_2^2 \approx \mathcal{O}(10^{16})$ remains by far the dominant one in the argument of the inner root operator compared to $h_1^2 \approx \mathcal{O}(10^{12})$. Again, it is critical that $\Delta\omega$ is so large for a

Xe system.

$$h_4 = \frac{1}{\sqrt{2}}\sqrt{-h_2 + \sqrt{h_1^2 + h_2^2}} \approx \frac{1}{\sqrt{2}}\sqrt{2\,\Delta\omega^2} = \Delta\omega \approx \mathcal{O}(10^4) \tag{S11}$$

We see that these two quantities determine the difference in the effective relaxation rates of the two pools (linked to the real part of f_{00} andf_{11}) and the difference in the observed frequencies (linked to the imaginary part of f_{00} and f_{11}, see Eq. 15).

$$f_{11}^{\mathrm{R}} - f_{00}^{\mathrm{R}} = h_3 \approx 0 \tag{S12}$$

$$f_{11}^{\mathrm{I}} - f_{00}^{\mathrm{I}} = h_4 \approx \Delta\omega \tag{S13}$$

For the case of large chemical shift differences, the effective relaxation rate is practically the same in both pools (since the exchange effect is dominant over the intrinsic relaxation rates) and the ultimately observed frequency difference is simply $\Delta\omega$.

The terms h_3 and h_4 are used to define further quantities which we need for the hyperbolic terms appearing in Baldwin's correction. Two parameters are

$$N = h_3 + i\,h_4 \approx i\,\Delta\omega \tag{S14}$$

$$N^* = h_3 - i\,h_4 \approx -i\,\Delta\omega \tag{S15}$$

and also $N\,N^* \approx \Delta\omega^2$. These are used to define (Eq. 36)

$$F_0 = \frac{\Delta\omega^2 + h_3^2}{N\,N^*} \approx \frac{\Delta\omega^2 + h_3^2}{N\,N^*} = 1 \tag{S16}$$

$$F_2 = \frac{\Delta\omega^2 - h_4^2}{N\,N^*} \approx \frac{\Delta\omega^2 - \Delta\omega^2}{N\,N^*} = 0 \tag{S17}$$

which still fulfills the general statement $F_0 - F_2 = 1$. Further definitions include (Eq. 41)

$$E_0 = 2\,h_3 \approx 0 \tag{S18}$$

$$E_1 = h_3 - i\,h_4 \approx -i\,\Delta\omega \tag{S19}$$

$$E_2 = 2\,i\,\Delta\omega \tag{S20}$$

These terms determine the argument of the $\sinh^{-1}$ which appear in p_{D} and $\nu_{1\mathrm{S}}$. We will now first show that the hyperbolic terms in $\nu_{1\mathrm{S}}$ vanishes in the case of the Xe@CrA-ma system. Evaluation of

$$\nu_{1\mathrm{S}} = F_0 \sinh(\tau_{\mathrm{CP}} E_0) - F_2 \sinh(\tau_{\mathrm{CP}} E_2) \approx 0 \tag{S21}$$

needs to consider that $F_0 \approx 1$ and $F_2 \approx 0$ while the arguments in the hyperbolic functions approach $\tau_{\mathrm{CP}} E_0 \approx 0$ and $\tau_{\mathrm{CP}} E_2 \approx 2\,i\,\tau_{\mathrm{CP}}\,\Delta\omega$. Here, it is critical that E_2 provides a complex argument. We can therefore use $\sinh(2\,i\,\tau_{\mathrm{CP}}\,\Delta\omega) \approx i\,\sin(2\,\tau_{\mathrm{CP}}\,\Delta\omega)$, which is a finite term between $-i, \ldots, i$ and F_2 causes the second term to disappear. With $\sinh(0) = 0$, we see that the first term also vanishes.

Next, we have to show that the second term in

$$p_{\mathrm{D}}\,N = \nu_{1\mathrm{S}} + (F_1^a + F_1^b) \sinh(\tau_{\mathrm{CP}} E_1) \tag{S22}$$

will also disappear. We use once more that the hyperbel function contains an imaginary argument and thus

$$\sinh(\tau_{\mathrm{CP}} E_1) \approx \sinh(-i\,\tau_{\mathrm{CP}}\,\Delta\omega) = i\sin(-\,\tau_{\mathrm{CP}}\,\Delta\omega) = -i\sin(\,\tau_{\mathrm{CP}}\,\Delta\omega) \tag{S23}$$

delivers a finite quantity. Its scaling factor $F_1^a + F_1^b$ reads

$$F_1^a + F_1^b = \frac{2\,\Delta\omega^2 - i\,h_1}{N\,N^*} \approx \frac{2\,\Delta\omega^2 - i\,2\,\Delta\omega\,k_{\mathrm{BA}}}{\Delta\omega^2} = \frac{2(\Delta\omega - i\,2\,k_{\mathrm{BA}})}{\Delta\omega} \approx 2 \tag{S24}$$

We note once more that this is an approximation where it is critical that the system is in “slow” exchange with dominant $\Delta\omega$. We can therefore summarize

$$p_{\mathrm{D}} \approx -\frac{2\,i}{N}\sin(\tau_{\mathrm{CP}}\,\Delta\omega) \approx -\frac{2\,i}{i\,\Delta\omega}\sin(\tau_{\mathrm{CP}}\,\Delta\omega) = \mathcal{O}(10^{-4}) \tag{S25}$$

Thus we see that for $p_{\mathrm{D}} \cdot k_{\mathrm{AB}} \to 0$ is fulfilled in the Xe host systems studied herein not only because exchange out of a dominant pool A is in general very infrequent but also because the dominant chemical shift suppresses p_{D}.

S1.5 Consistency with the General N-Site Exchange Description

A general description for experimental data from CPMG measurements has been introduced recently by Koss *et al.* [12], including N pools with variable size, and covering the full dispersion range from slow to fast pulsing with applicability to the full range of exchange kinetics. Its eq. 29 yields the exchange contributions for N = 2 in slow exchange as

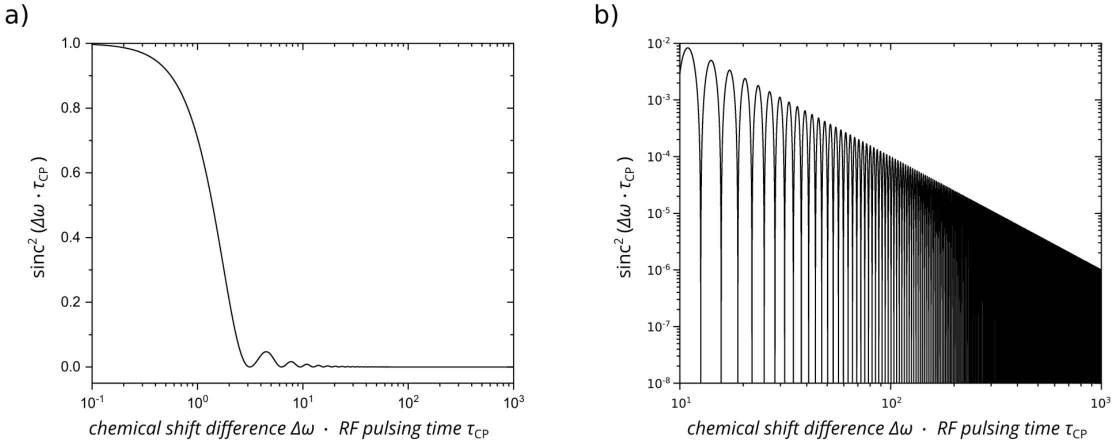

Figure S2: Plot of the sinc^2 term in the generalized description of 2-site exchange by Koss *et al.* [12] in the slow exchange limit. a) Overview, b) zoom into the range of $\Delta\omega \cdot \tau_{\mathrm{CP}} \approx 10^2$ for the chemical shifts occurring in this study and echo times on the order of 10 ms.

$$R_{2,\text{ex}} = \frac{p_\text{A} \cdot p_\text{B} \cdot k_\text{ex}^2 \left[1 - \text{sinc}^2(\Delta\omega \cdot \tau_\text{CP}) + p_\text{B} \cdot k_\text{ex} \cdot \Delta R_{2,\text{AB}}\right]}{k_\text{ex} + \Delta R_{2,\text{AB}}} \tag{S26}$$

with p_A, p_B being the normalized fractional pool sizes ($p_\text{A} + p_\text{B} = 1$; their notation called population) and $\Delta R_{2,\text{AB}}$ being the difference in the intrinsic relaxation rates in both pools. The product $p_\text{A} \cdot p_\text{B}$ can be approximated in our case by f_B. The argument in the sinc^2 term is on the order of 10^2, such that the term itself is on the order of 10^{-4}, as shown in Figure S2. The last term, $p_\text{B} \cdot k_\text{ex} \cdot \Delta R_{2,\text{AB}}$ is also negligible because of the small p_B and small $\Delta R_{2,\text{AB}}$ whereas k_ex is not excessive. As the denominator also reduces to k_ex, the whole fraction simplifies to $f_\text{B} \cdot k_\text{ex} \approx f_\text{B} \cdot k_\text{BA}$ as used in the main manuscript.

S1.6 Insights from Saturation Transfer Experiments

A crucial aspect of our theoretical description are the simplifications that come with $\Delta\omega$ being the dominant item in all terms contributing to $R_{2,\text{eff}}$. However, $\Delta\omega$ is not necessarily known *a priori* and can become inaccessible in direct ^{129}Xe NMR spectra: for example, observing the direct peak of pool B requires relative large concentrations, which in turn shortens $T_{2,\text{eff}}$ for systems with $\Delta\omega \approx 10^4\,\text{s}^{-1}$ so dramatically that the signals suffer from significant line broadening or effects of increasing coalescence when approaching the fast exchange regime. An independent method such as Hyper-CEST is therefore the key to qualitatively verify the assumptions which have been made. However, the end result will be independent of $\Delta\omega$ and allow an accurate quantification of the exchange rate or gas turnover.

We have shown previously that quantitaive analysis of the saturation transfer allows to derive values for k_BA and f_B [1]. The observed signal loss is dominated by the actively driven CEST effect for a system like CrA-ma in water or DMSO, and thus, by choosing proper saturation conditions, $T_{2,\text{eff}}$ relaxation effects in pool B can be neglected for CEST. This can be seen from the theoretical description for the driven depolarization (Ref. [2, 1]) and includes the transverse relaxation in the CEST pool as follows (here, the only approximation used is that $\Delta\omega$ is dominant compared to all other rates; this can be confirmed retrospectively when investigating an uncharacterized system):

$$\lambda_\text{max} = f_\text{B} \cdot k_\text{BA} \cdot \frac{\omega_1^2}{\omega_1^2 + k_\text{BA} \cdot (k_\text{BA} + R_{2,\text{B}})} \tag{S27}$$

Achieving a strong, narrow CEST response with no excessive saturation power will then give important insights. Here, it is important to understand why λ_max is sufficiently large and how this is seen in the context of the entire CEST spectrum, *i.e.*, the width of the response. The driven depolarization should be efficient because of $f_\text{B} \cdot k_\text{BA}$, *i.e.*, a sufficiently large CEST pool and a fast release of saturated magnetization into the detected bulk pool. A high saturation power, ω_1, helps to achieve the upper limit of λ_max, namely $f_\text{B} \cdot k_\text{BA}$ when ω_1^2 becomes the dominant term[1, 9]. However, ω_1, should not be excessive, as it causes detrimental line broadening. Overall, the saturation power should be sufficient such that ω_1^2 is comparable with k_BA^2 in the denominator. In such cases, it ensures that saturation occurs fast enough compared with k_BA, *i.e.*, before many spins leave the CEST pool. Any further increase is problematic because the line width

$$\Gamma = 2\sqrt{\frac{k_{\mathrm{BA}} + R_{2,0}}{k_{\mathrm{BA}}}\omega_1^2 + (k_{\mathrm{BA}} + R_{2,\mathrm{B}})^2} \tag{S28}$$

increases linearly with ω_1 for excessive saturation power. We have shown for the initial characterization of CrA-ma in DMSO that a sharp CEST response could be achieved for $B_1 = 1.1\,\mu\mathrm{T}$, *i.e.*, $\omega_1 \approx 12.9\,\mathrm{Hz}$[1] at r.t. . Further tests showed that a saturation power of ca. $4\,\mu\mathrm{T}$ gives already 50 % of the maximum possible depolarization rate[9]. Hence, a characteristic rate of $\omega_1 \approx \mathcal{O}(10^2)\,\mathrm{s}^{-1}$ is sufficient to drive the depolarization. At the same time, the observed CEST line width at $\Delta\omega = 166$ ppm offset from pool A was not dominated by $R_{2,\mathrm{B}}$ and thus the upper limit for relaxation in the CEST pool must be $R_{2,\mathrm{B}} \leq \mathcal{O}(10^2)$. This is also consistent with simulations of the CrA-ma system that used relaxation rates of $R_{2,\mathrm{B}} \leq 500\,\mathrm{s}^{-1}$.[2] We thus see that $\Delta\omega \gg R_{2,\mathrm{B}}$.

S1.7 Relaxation Dispersion Simulation

For isolating the exchange contribution, one typically needs to compare fast pulsing observations with slow pulsing results. The Swift-Connick treatment yields the extreme limit of the latter case but line width analysis is often masked by other line broadening. Hence, the CPMG method is used to eliminate other R_2 effects and isolate the exchange contribution.

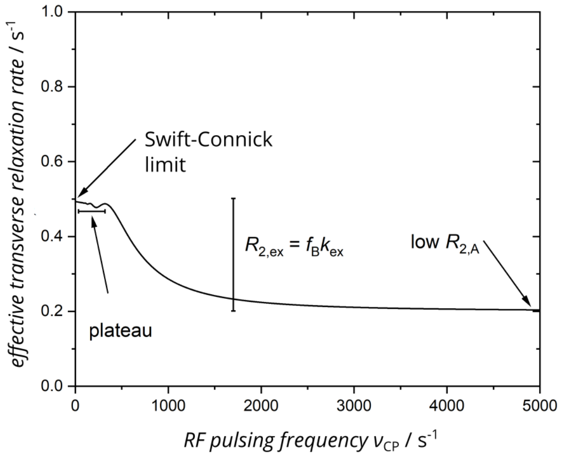

Figure S3: Simulation of relaxation dispersion with dominant but not yet excessive chemical shift difference $\Delta\omega$ (fix simulation parameters: total exchange rate $k_{\mathrm{ex}} = 300\ \mathrm{s}^{-1}$, chemical shift difference $\Delta\omega = 2000$ Hz, fractional size of pool B $f_\mathrm{B} = 0.001$, and $R_{2,\mathrm{A}} = R_{2,\mathrm{B}} = 0.2\ \mathrm{s}^{-1}$).

For slow exchange, we saw that the exchange contribution is given by $f_\mathrm{B} \cdot k_{\mathrm{ex}}$. Figure S3 illustrates that one aims for a large step size $R_{2,\mathrm{ex}}$. But this requires a) high k_{ex} or b) large f_B (best: both). Large f_B requires a lot of material and some simplifications do not apply any more in this case. Large k_{ex} (which is particularly important if the B pool is very dilute) comes with the risk that one approaches the fast exchange limit. Xe now offers large $\Delta\omega$ such that even relative high exchange rates are still in the "slow exchange regime". Moreover, Xe has low R_2 to start with. This makes it possible to identify differences in the signal decay once the (small) B pool is present. An exchange contribution of 0.1 s^{-1} is easier to identify in slow decaying echoes than in fast decaying echoes. Figure S4 illustrates the normalized signal difference when comparing two signal decays differing by R_{ex}.

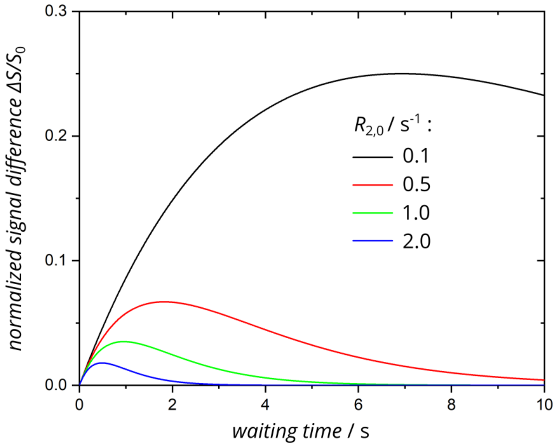

Figure S4: Signal difference for exponentially decaying signals with various initial decay constants (fix simulation parameter: exchange-induced transverse relaxation rate R_{ex} = 0.1 s^{-1}).

To measure the full R_{ex}, one needs to reach the plateau for high relaxation in the slow pulsing limit. But this is challenging because fast decaying signals should be sampled with short echo times, hence fast pulsing. Figure S5 illustrates that we benefit again from the large $\Delta\omega$ because it shifts the dispersion curves far to the right.

Once the $\Delta\omega$ is just 10 times larger than the k_{ex} of 300 Hz, one remains in the plateau for up to 200 Hz pulsing frequency. Any larger $\Delta\omega$ makes it even easier to apply short echo times but still measure the full exchange contribution. Another aspect is to which extend a small f_{B} is beneficial for this case or not. Technically, f_{B} increases the step size for the maximum exchange contribution to the relaxation as shown in Figure S6. Increasing f_{B} would make it easier to quantify the exchange contribution with higher accuracy, but we do not need this for Xe with the convenient k_{ex}. A small f_{B} together with large $\Delta\omega$ simplifies handling of the intrinsic relaxations according to the condition $|R_{2,0} - R_{2,\text{B}}| \ll \Delta\omega(f_{\text{A}} - f_{\text{B}})$: Changing the f_{B} mainly scales the step size but does not shift the curve horizontally or changes the transition area such that one might accidentally sample outside the plateau once the concentration of the B pool changes. Increasing f_{B} by a factor of x increases the step size accordingly. Taking $\Delta R = R_{2,\text{eff}} - R_{2,0}$ for two different pool B magnitudes, $f_{\text{B},2} = x \cdot f_{\text{B},1}$ (the latter set to 0.001) one can investigate the two functions ΔR for $f_{\text{B},1}$ and $\Delta R'$ for $f_{\text{B},2}$. These can be compared as $\Delta R/(x\Delta R')$ to see

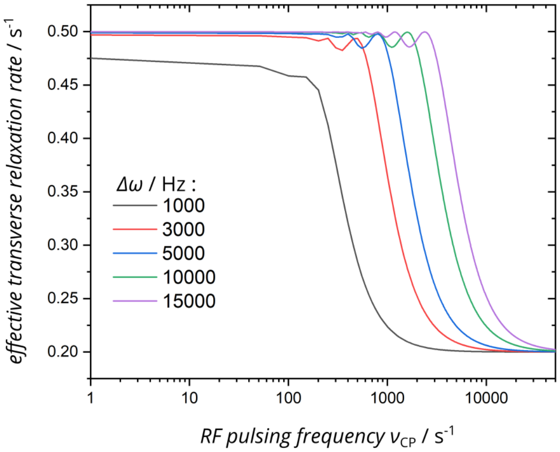

Figure S5: Simulation of relaxation dispersion with increasing chemical shift difference $\Delta\omega$ (diamagnetic extreme limit: $\Delta\omega > 10$ Hz; fix simulation parameters: total exchange rate $k_{\text{ex}} = 300$ s^{-1}, and fractional size of pool B $f_{\text{B}} = 0.001$).

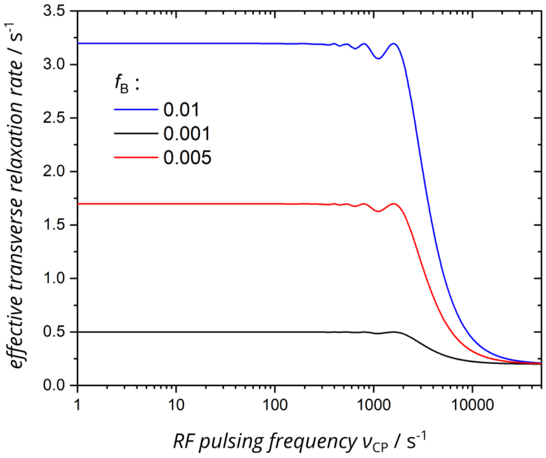

Figure S6: Simulation of relaxation dispersion with a variable fractional size of pool B (fix simulation parameters: total exchange rate $k_{\text{ex}} = 300$ s^{-1}, chemical shift difference $\Delta\omega = 10$ kHz, and $R_{2,\text{A}} \; = \; R_{2,\text{B}} = 0.2$ s^{-1}).

if the larger $f_{\mathrm{B},2}$ just causes a scaling of the R_2 component that increases when approaching the slow pulsing limit (moving from right to left in the dispersion plot). Figure S7 is the plot of $\Delta R/(x\Delta R')$ to confirm this simple scaling over a large range of the plateau region.

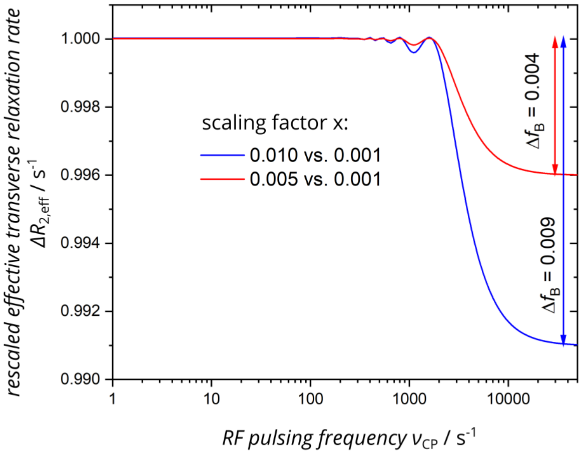

Figure S7: Comparing the step sizes for dispersion curves from different f_B conditions after re-scaling and plotting them as $\Delta R/(x\Delta R')$.

This plot means that increasing the f_B 5-fold from 0.001 to 0.005 scales the plateau by a factor of 5. For the transition and the fast pulsing limit towards slow relaxation, the scaling factor 5 is not 100 % correct. Interestingly, it is off by another factor that eventually corresponds to the difference of $f_{\mathrm{B},2}$ and $f_{\mathrm{B},1}$, hence $\Delta f_\mathrm{B} = |f_{\mathrm{B},2} - f_{\mathrm{B},1}| = f_{\mathrm{B},1}(x-1)$. This is more a side note but it shows that changing f_B never gives the risk to shift the transition region of the dispersion curve. A similar effect as for an increasing f_B is also observed for an increase in k_BA, at least between 100 and 1000 Hz as long as $f_\mathrm{B} \cdot k_\mathrm{ex}$ is dominated by $\Delta\omega$. Considering eq. 4-7 used by Millet *et al.*, we see that the increase in k_ex is dominated everywhere by $\Delta\omega$, except in the final $R_{2,\mathrm{ex}}$ equation. Figure S8 illustrates simulations for increasing exchange rates over the full range from the slow to the fast regime.

S2 Undersampled MR-Image Reconstruction

Radial sampling has the advantage that each readout line captures signal for the center of k-space and can thus contribute to evaluating the signal decay. However, the numbers of projections, p, for Nyquist-Shannon artifact-free MR image reconstruction (p = matrix size $\cdot\pi/2$) is *per se* larger than the number of readouts in Cartesian sampling. A larger matrix size thus increases the minimum possible spin echo time and causes the effective echo time for an individual scan to be less sharp defined.

In Figure S9, each ^{129}Xe image shows the very first image of the image series stack of the very same sample phantom (both compartments contained DMSO, but only the inner compartment

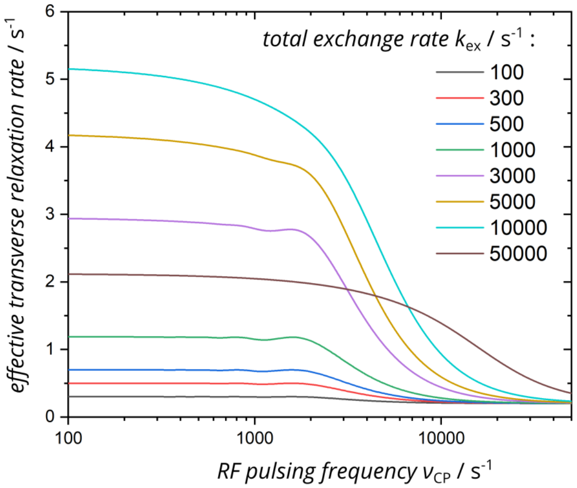

Figure S8: Simulation of relaxation dispersion with a variable exchange rate (fix simulation parameters: fractional size of pool B f_B = 0.001, chemical shift difference $\Delta\omega$ = 10 kHz).

additionally 50 μM of CrA-ma). Additionally, the matrix size was varied. All scans were recorded with Golden Angle-based (GA) radial sampling.

In contrast to conventional uniform radial k-space sampling, GA-based radial sampling acquires projections in time which will never overlap with any of the prior acquired projections. Thus, it does not contain any redundant k-space information. It's irrational angle is given by $\varphi_{\mathrm{GA}} = 180°/\gamma_{\mathrm{GA}}$ where $\gamma_{\mathrm{GA}} = (\sqrt{5}+1)/2 = 1.618034\ldots$ is known as the Golden Ratio or Golden Section and solves the equation $\gamma_{\mathrm{GA}}^2 = \gamma_{\mathrm{GA}} + 1$ (thus; $\varphi_{\mathrm{GA}} = 111.246\ldots°$) [13]. The Golden Ratio is achived as the ratio of adjacent Fibonacci numbers, $F(k) = \{1, 1, 2, 3, 5, \ldots\}$ with recursive Fibonacci function $F(k+2) = F(k+1) + F(k)$ [13]. Taking the GA-based approach adds the following three advantages over uniform radial sampling into the system: 1) Each newly added projection divides in k-space the largest azimuthal gap; 2) If the number of projections is equal to a Fibonacci number, then only two different azimuthal gaps occour; 3) As the sampling scheme is based upon a constant angle increment, a window that is temporally moving or "sliding" by n·TR (repetition time) selects a constant sampling pattern that is rotated by a constant increment of $\varphi = n \cdot \varphi_{\mathrm{GA}}$[13].

GA-based radial k-space sampling was proposed for ^{1}H-MRI and is capable for dynamic studies capturing fast signal changes [13]. In addition, quantitative mapping of T_1, T_2, and spin-density has also been demonstrated for ^{1}H-MRI with GA-based radial sampling [14, 15].

The reconstructed HP ^{129}Xe MR images in Figure S9 were obtained with either of the following three methods:

A) fully sampled data (according to Nyquist-Shannon: projections=matrix size$\cdot\pi/2$) and conventional NUFFT reconstruction;

B) undersampled acquisition using only 8 projections and conventional NUFFT reconstruction;

C) same undersampling with 8 projections as for B), but using our proposed smoothed KWIC (sKWIC) NUFFT reconstruction (details given in next section S2.2).

If $T_{2,\text{eff}}$ is too fast and the MR imaging method too slow, then mixed contrast arises in the image and the quantification of any $T_{2,\text{eff}}$ contrast becomes less accurate. The effective signal contrast in the area with the Xe binding partner has varied significantly during the time period needed for full Nyquist-Shannon amount of data recording and only an averaged effect shows up as image contrast.

When reconstructing the MR-image for the very first time point possible, the disadvantage of conventional fully sampling (top row) became evident as mixed contrasts (red arrows in Figure S9), in particular for higher matrix sizes where the $T_{2,\text{eff}}$-decay happens on a scale that is faster than the total acquisition time of the MR image. These mixed contrasts impact $T_{2,\text{eff}}$ accuracy. For the MR images that were reconstructed from only 8 projection (middle row), the mixed contrast is greatly minimized (red arrow), at the expense of streaking artifacts. These streaking artifacts can be removed using the sKWIC filter (bottom row).

S2.1 k-Space Weighted Image Contrast (KWIC)-Filter Design

The k-space weighted image contrast (KWIC) filter is similar to the keyhole concept on Cartesian k-spaces, but with (at least) the following two differences:

1. KWIC is for radial k-space sampling;
2. KWIC cuts out parts of already taken data similar to a mask.

Therefore, similarly to the Cartesian keyhole concept, radial sampling with KWIC filter reconstruction focuses on the center of k-space only, but in a much more flexible fashion being able to further widen or narrow retrospectively the width of the “temporal MR reconstruction window” on already taken data [13]. To add even more flexibility to the KWIC filter, the “diameter” of each Nyquist ring can also be set/adapted to match either the Nyquist criterion or to be narrower for oversampling or wider for undersampling, respectively.

The KWIC filter [13, 15, 14] makes heavy usage of GA-based radial sampling pattern. For simplicity, the KWIC filter shown in Figure S10 is described only for the first frame, but the principle applies also for the other frames. After 90° RF excitation, the intensity of the transverse magnetization decays with the total transverse relaxation time, T_2 (Figure S10; red curve; $T_{2,\text{eff}}$ decay).

Following the data density in radial k-space sampling starting from the center of k-space radially to the outer k-space, the data is oversampled at the k-space center, Nyquist sampled at the Nyquist radius, and undersampled beyond the Nyquist ring in the outer k-space. Thus, radial k-space sampling is highly non-uniform.

We wanted to take only a small number of projections for MR-image reconstruction to follow the signal decay and contrast build-up in time as closely as possible by using – for the purpose of simpler illustration – only the first 5 full projections (for real, we used 8 projections).

As this is highly undersampled regarding the matrix size of the MR-image, the reconstructed image has streaking artifacts (compare Figure S9; middle row). To remove such streaking artifacts arising from undersampling, but to preserve the MR-image contrast contribution from

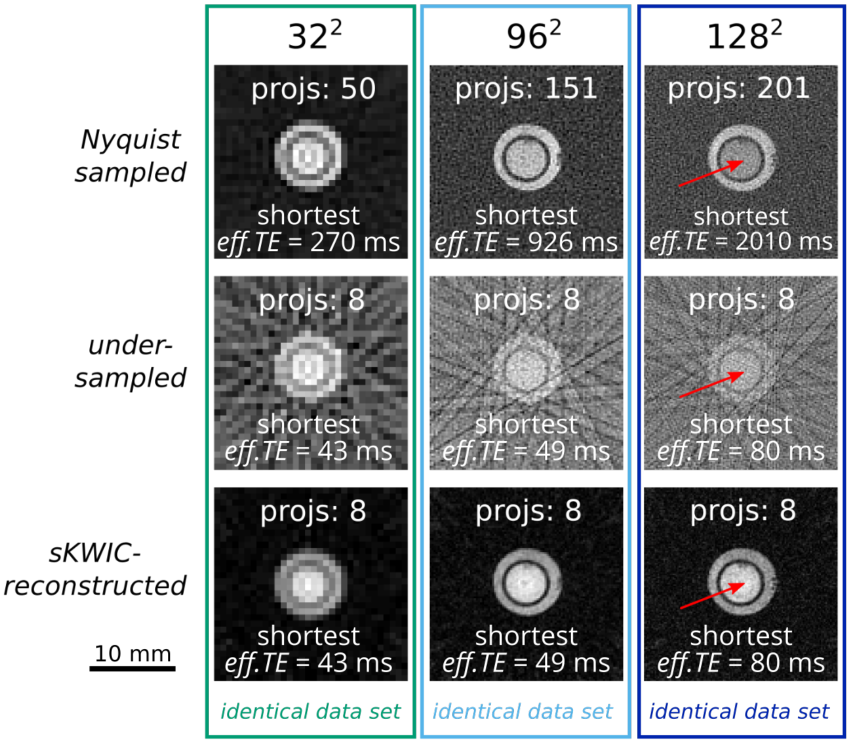

Figure S9: Comparison of Nyquist sampled (top row), undersampled (8 projections) data with conventional reconstruction (middle row), and undersampled (8 projections), but sKWIC reconstructed data (bottom row) of Golden-Angle (GA) based radial sampling for different matrix sizes ($TE(32^2)$ = 10.82 ms; $TE(96^2)$ = 12.27 ms; $TE(128^2)$ = 20.00 ms) on the very same sample (field-of-view: 20×20 mm^2). Only the inner compartment of the double phantom contained 50 μM of CrA-ma. Note: of all images shown here, each is always only the first of the MR image series stack that corresponds to the first possible reconstructed time point; thus, each image represents the beginning of the $T_{2,\text{eff}}$ signal decay curve and should not yet show any darkening in the MR signal because of the presence of CrA-ma. However, a contrast became more and more apparent the larger the matrix size was when time consuming full Nyquist sampling was used (top row; red arrows). Both undersampled methods (middle and bottom row) do show correct contrast behavior in the presence of CrA.

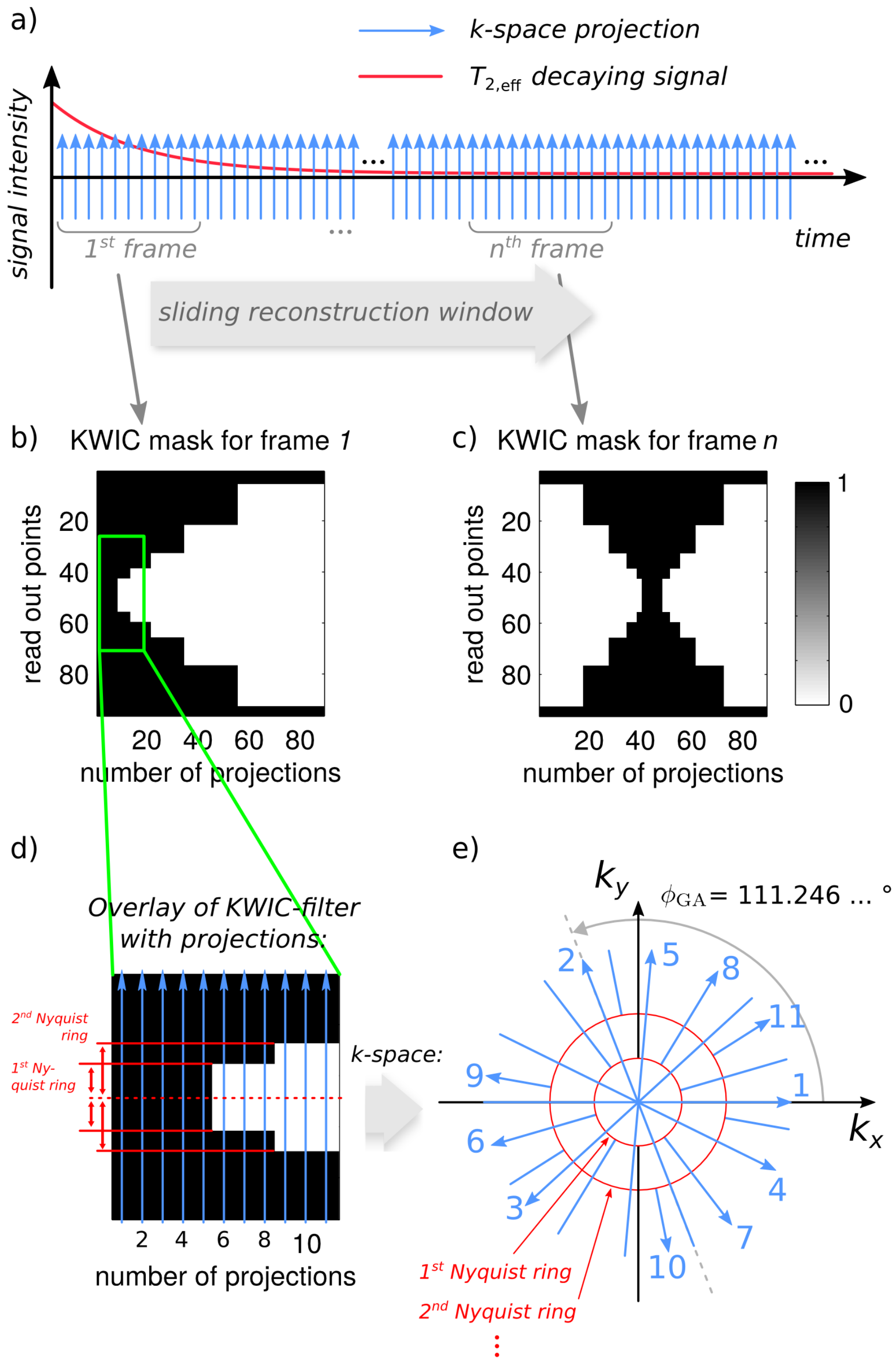

Figure S10: Illustration of KWIC-filter design for a matrix size of 96 × 96.

only these 5 projections, the KWIC filter defines Nyquist rings at which adjacent projections are added to fill up the undersampled outer k-space, but their central part corresponding to the center of k-space is cut-off (see KWIC mask: white = 0; black = 1; this corresponds to the projections no. 6, 7 and 8 in Figure S10d and Figure S10e). This procedure is continued by a second Nyquist ring by which the k-space including the newly added projections starts to become again undersampled and is filled up again, but now using projections 9, 10 and 11. This is repeated until the required k-space is completely filled. By this procedure, no contrast will be added into the reconstructed MR-image by adding projections from later time points, but also undersampling artifacts will be removed. In total, the main signal and contrast of the first reconstructed image is mainly given by the signal of the initial 5 projections 1 to 5.

For any later reconstructed frame, the center of the KWIC-filter, which keeps the projections untouched, shifts until the asymmetric KWIC-filter becomes symmetric and slides as a reconstruction window to later time points (Figure S10c).

S2.2 KWIC versus smoothed KWIC Reconstruction

Sharp edges in k-space (as generated from the Heaviside step function used in the conventional KWIC filter) introduce Gibbs-ringing in MR images after Fourier-transformation. To reduce these artifacts and therefore to further increase the SNR, we smoothed these sharp edges of the Heaviside step function in a first approximation by linear smoothing (smoothed KWIC; sKWIC; Figure S11).

The sKWIC filter was designed such that a linear function with a particular slope smoothed the step of the conventional KWIC filter. We used the following slopes for each Nyquist ring transition:

2nd Nyquist ring: readout points: 7 → slope: 1/7 = 0.143 per readout point.
3rd Nyquist ring: readout points: 5 → slope: 1/5 = 0.2 per readout point.
4th Nyquist ring: readout points: 7 → slope: 1/7 = 0.143 per readout point.
5th Nyquist ring: readout points: 12 → slope: 1/12 = 0.083 per readout point.
6th Nyquist ring: readout points: 17 → slope: 1/17 = 0.059 per readout point.

Critically, up to 20 % of noise in the reconstructed MR image could be reduced using the smoothed KWIC filter approach (see color- and gray-scale difference image in Figure S11). The correct functionality of the sliding reconstruction window is illustrated in Figure S12 for increasing echo times. This Fig. also illustrates the impressive benefits of this approach for obtaining high spatial resolution without loosing the ability to include high temporal resolution and the feature of short overall acquisition times.

For relaxation time mapping, Figure S13 compares fitting results obtained from KWIC and sKWIC reconstructed MR images ($T_{2,\text{eff}}$, M_0 and standard errors). The standard deviations are significantly reduced with sKWIC.

S3 $T_{2,\text{eff}}$ Evaluation Procedure

For relaxivity mapping, a consistency check was performed with the two-compartment phantom containing the same sample (DMSO) in both volumes. Fig. S14 shows that a homogeneous

KWIC-filter

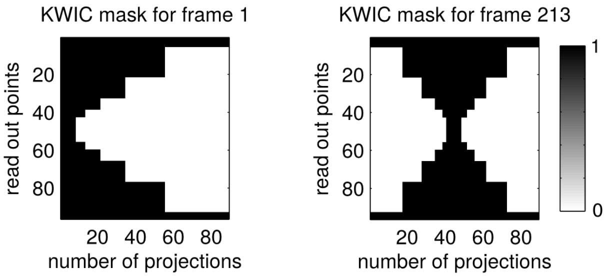

smoothed KWIC (sKWIC)-filter

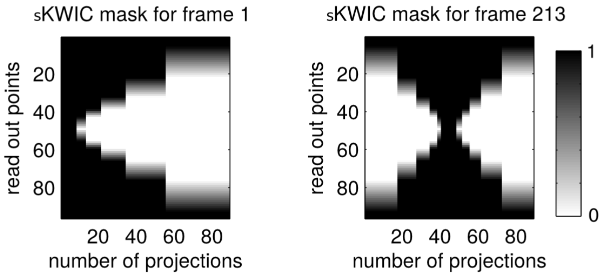

Noise reduction in reconstructed MR-image:
KWIC- versus smoothed KWIC-filter:

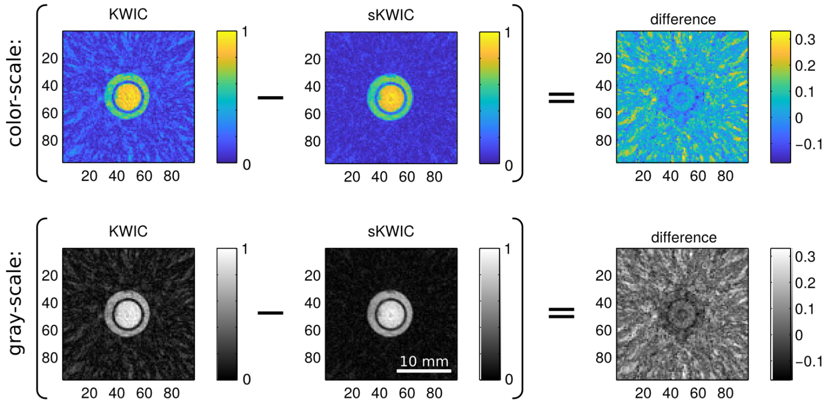

Figure S11: KWIC versus smoothed KWIC (linear function at the edges of Nyquist rings) reconstruction with identical parameters (shown for frame 1 (left) and frame 213 (right)). To compare its differences, the same data were either KWIC or sKWIC filter reconstructed and its corresponding MR images were subtracted from each other; revealing over 20 % of reduced noise when using sKWIC (bottom; either color map (top), or gray map (bottom)).

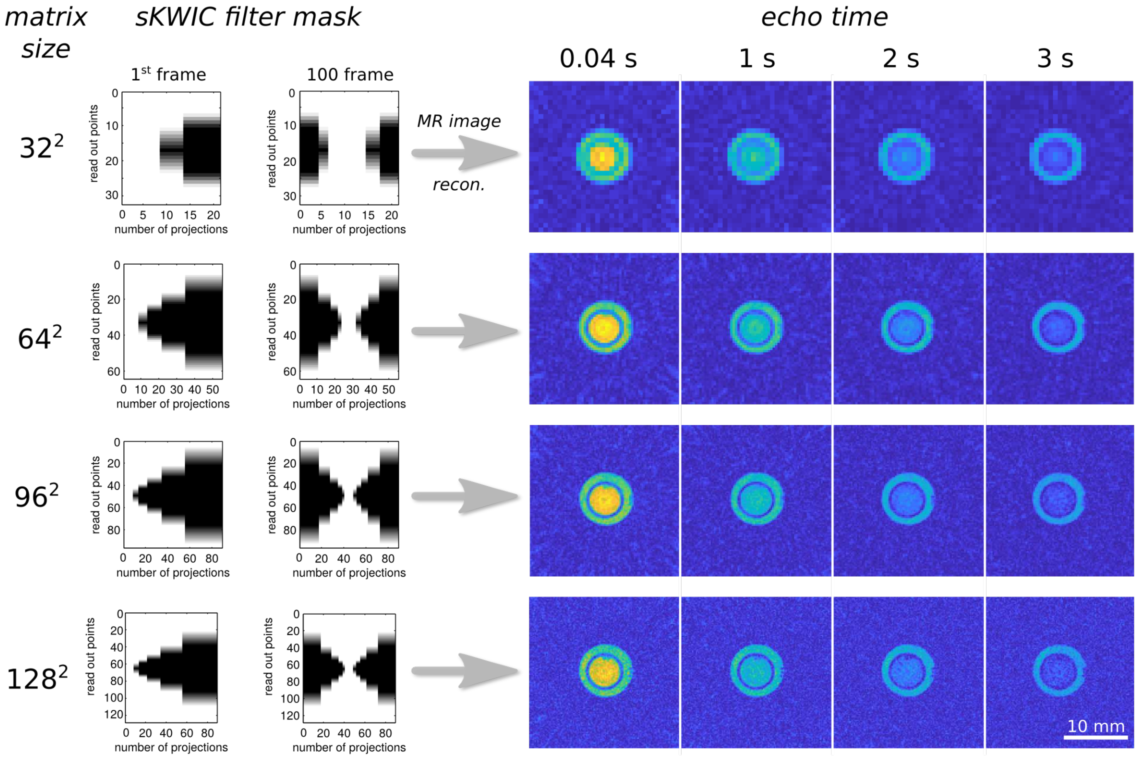

Figure S12: sKWIC filter masks and reconstructed ^{129}Xe MR images for different matrix sizes. The asymmetric sKWIC filter was used to reconstruct the first frame at 40 ms of spin echo time. As the filter slides along the time dimension for reconstructing images for larger TE, it gradually changes its shape towards the symmetric shape as exemplary shown here for frame 100; and echo times of 1 s, 2 s, and 3 s. Sample: DMSO in both compartments, only the inner compartment contained 50 μM of CrA-ma additionally; T=295 K. At matrix sizes larger than 96^2 (at field-of-view of 20×20 mm^2), the glass capillaries started to become spatially resolved.

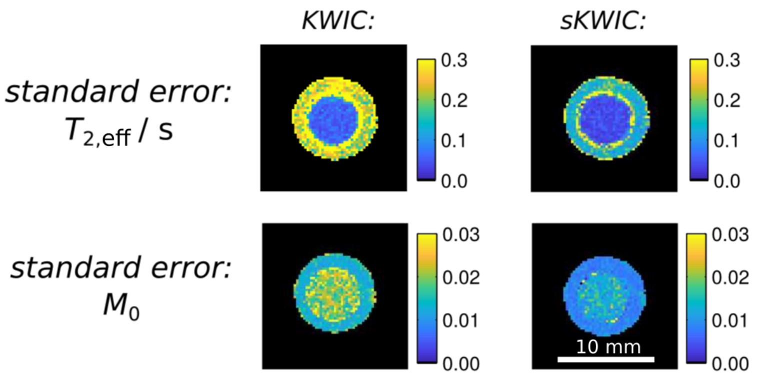

Figure S13: KWIC versus smoothed KWIC reconstruction impact on the errors of $T_{2,\mathrm{eff}}$, and M_0 quantification/fitting.

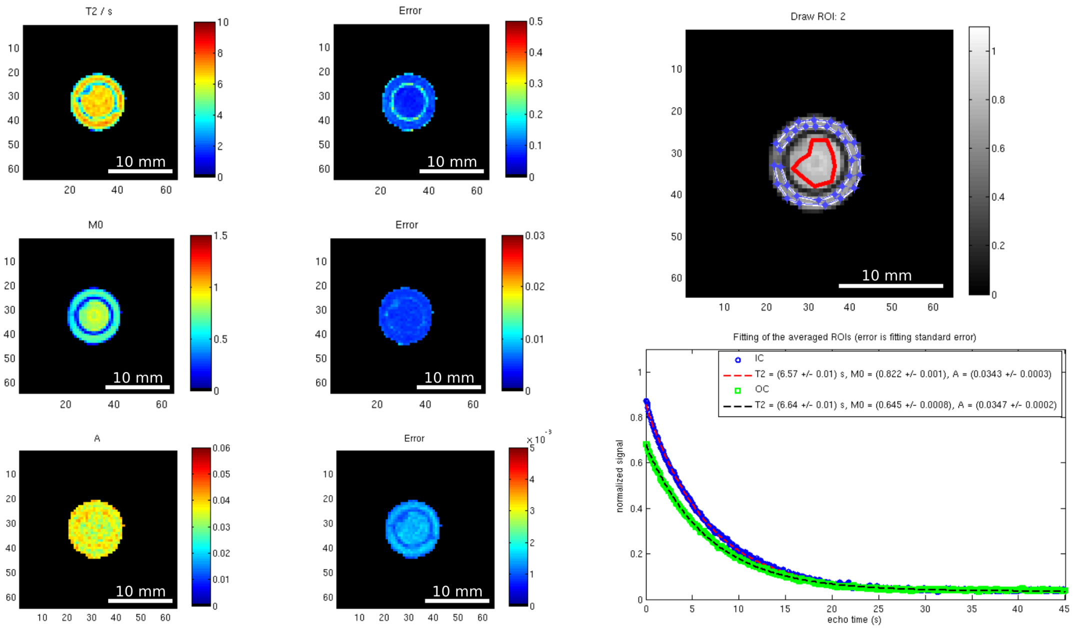

Figure S14: Consistency check with double-compartment phantom (no CrA-ma in either compartment); T = 303 K. The method yields a homogeneous $T_{2,\mathrm{eff}}$ throughout both physically separated compartments. Due to the low noise level, all data can be included into the fitting procedure (field-of-view of $20\times20\,\mathrm{mm}^2$).

result for the decay constant and starting magnetization is obtained throughout the two volumes.

In a second consistency check, we removed the inner NMR tube and studied a single solution with 150 μM CrA-ma with different matrix sizes and RF pulse combinations. The results for $T_{2,\text{eff}}$ are given in Tab. S1.

The $T_{2,\text{eff}}$ errors in Table S1 were derived by the following three procedures and were listed in that order:

1. A pixel-wise $T_{2,\text{eff}}$-fit was done throughout the image series and the standard deviation of the $T_{2,\text{eff}}$ map values within a ROI were taken. This represents the scattering of the individual $T_{2,\text{eff}}$ values (without considering the standard deviations from the individual fits) and represents the largest uncertainty.

2. A new error is calculated from the individual standard errors of *lsqcurvefit* obtained by *Nlparci* using the residual and the Jacobian of each pixel of the $T_{2,\text{eff}}$ map.

3. Standard error as in 2), but fitting only one signal decay obtained from the ROI averaged signal along the time series (instead of fitting a signal decay for each individual pixel). This yields the smallest errors.

We see from Table S1 that the transverse relaxation time was not significantly influenced by the chosen combination of RF excitation/refocussing pulse shape both the Gauss/Gauss (G/G) or Hermite/Mao (H/M), have comparable results. However, comparing the data in Tab. S1 for different matrix sizes gave the impression that the increased matrix size yields consistently lower values for $T_{2,\text{eff}}$. It is indeed possible that signal decay rates are systematically higher for larger matrix sizes (though the values still agree within the error bars of the scattering within the $T_{2,\text{eff}}$ map). A possible explanation is that images with larger matrix size, hence smaller pixels, are more susceptible to diffusion effects: a certain fraction of spins leaves the encoded pixel during the echo train and thus an enhanced signal loss is observed. This diffusion effect causes, however, only a constant offset that does not affect the slope within a concentration series that is studied with a fixed matrix size. The relaxivity r_2 determined from the slope remains practically unaffected. Whereas this is convenient for the exchange dynamics parameters derived in this study, the simple $T_{2,\text{eff}}$ determination should keep this effect in mind. Another side effect of increased matrix size is that the minimum echo spacing is slightly increased (overall range for all matrix sizes: 11 ms to 17 ms). While this technically represents a reduction in ν_{CP}, we do not consider this as a real dispersion effect since a) our simulations showed that the conditions for Xe should not show a dispersive behavior in this regime and b) it would only be a small shift towards slow pulsing.

Along with these consistency checks we noticed that fitting the signal decay for individual pixels has to be done with care when judging individual $T_{2,\text{eff}}$ values. The signal (and thus the sign) of the reconstructed magnitude MR images was always positive in our case and because of that, this *offset* can bias the $T_{2,\text{eff}}$ values obtained by fitting (see Figure S15). This is important when evaluating the signal decay from a single pixel because the noise level is high: we considered for fitting only the first data points that were outside one standard deviation (horizontal blue dashed line) of the mean of the *offset* (horizontal blue solid line). We also considered throwing out even more data by taking only the first data outside twice the standard deviation of the mean of the *offset* (horizontal red dashed line), but this did not changed the obtained

Table S1: Within error limits, the change in quantified transverse relaxation time was not impacted by the RF excitation/refocussing pulse pair Gauss/Gauss (G/G) or Hermite/Mao (H/M). Further explanation regarding the different error bars is given in the text.

matrix size	RF pulse shape pair	$T_{2,\text{eff}}$ / ms	aqc. time / s
32^2	G/G	$468 \pm \{50,20,3\}$	$\approx$15
32^2	H/M	$440 \pm \{30,10,3\}$	$\approx$15
64^2	G/G	$427 \pm \{100,40,4\}$	$\approx$15
64^2	H/M	$397 \pm \{80,30,3\}$	$\approx$15

fit result for $T_{2,\text{eff}}$ (see histogram analysis in Figure S15b). We therefore kept the one standard deviation criterion (blue) for the main manuscript.

Regarding image contrast, the best contrast between fast relaxing and slow relaxing species is determined as follows: Between two neighboring compartments having fast (F) and slow (S) $T_{2,\text{eff}}$ decay, we find the echo time for maximal contrast (assuming that both give about the same signal intensity of *offset*: $\mathit{offset}_F \approx \mathit{offset}_S$) by solving:

$$0 = \frac{\partial}{\partial t}\left[\{M_{0,\text{S}} \cdot e^{-t/T_{2,\text{s}}}\} - \{M_{0,\text{F}} \cdot e^{-t/T_{2,\text{F}}}\}\right]_{t=TE_{\text{MC,ana}}}$$

The (spin echo-) time for maximum contrast found analytically is given by

$$TE_{\text{MC,ana}} = \frac{T_{2,S} \cdot T_{2,F}}{T_{2,S} - T_{2,F}} \cdot \ln\left(\frac{T_{2,S} \cdot M_{0,F}}{T_{2,F} \cdot M_{0,S}}\right) \tag{S29}$$

S3.1 Acceleration of Data Collection and Reduced Xe Deliveries

For NMR studies working with hyperpolarized nuclei, one has to consider that these need to be delivered into the sample. This takes time and is not necessarily easy to repeat for multiple measurements. Thus, using the available magnetization as efficient as possible is an important concern. Thus, subsampling techniques can save time and material. The corresponding gold-standard Cartesian rapid acquisition with relaxation enhancement (RARE) measurement for $T_{2,\text{eff}}$ mapping requires for each phase encoding step (which is proportional to the matrix size of the image) a delivery of new, fresh hp Xe (given that no segmentation mode is used). Let us consider a matrix size of 32^2: If each new spin echo is arranged as one line in k-space for $T_{2,\text{eff}}$ measurement, then 32 deliveries of fresh, hp Xe are required. This results in ca. 992 s = 15.4 min in total acquisition time (using an echo time spacing of 400 ms per phase encoding step; 50 echo images; Xe bubbling time of 10 s and a bubble collapse time of 1 s; thus, in sum a repetition time of 31 s per phase encoding step). In contrast, a total acquisition time of less than 31 s was required for the single-shot GA-based radial RARE measurement (in detail: Xe bubbling time: 10 s; a bubble collapse time of 1 s; and continuous data recording time of 20 s). This yields a ca. 32-fold acceleration in data acquisition. Similarly, the total acquisition time for matrix sizes of $64^2/96^2/128^2$ using the same considerations would be ca. 33 min/50 min/66 min for conventional Cartesian encoding. The proposed single-shot GA-based approach yields a 64-fold/96-fold/128-fold acceleration, respectively.

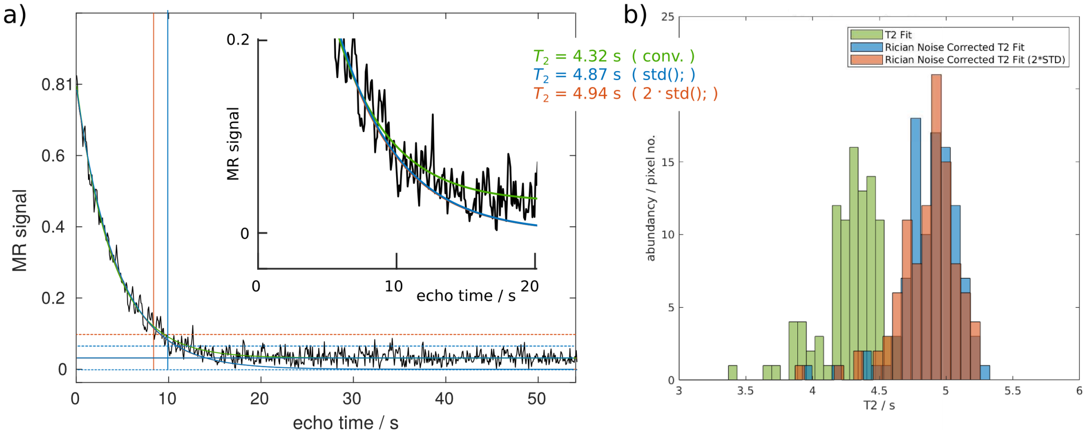

Figure S15: a) Green curve: conventional $T_{2,\text{eff}}$ fit ($S(t) = M_0 \cdot e^{-t/T_{2,\text{eff}}} + \textit{offset}$) taking all data; blue: our improved $T_{2,\text{eff}}$ fit that takes only the first data that is above the standard deviation (horizontal blue dashed line) of the mean of *offset* (horizontal blue solid line); red: same as blue, but taking even less data that are twice the standard deviation (horizontal red dashed line) above mean of *offset*. b) Histogram comparing these three fit approaches on the same MR image data set.

S4 Quantitative Saturation Transfer Results

To validate the exchange rate that was determined with Equation (4) in the main manuscript, quantitative Hyper-CEST[1] was used for similar range of temperature (Figure S16). The absolute chemical shift of free Xe in solution showed a plateau behavior; this is in excellent agreement (for the temperature and ppm ranges used in our study), for approaching actually a maximum with temperature, which has been discussed in literature [16]. Also, a parabolic behavior of the Xe solubility with temperature was also reported by Clever[17]. The concentration of dissolved Xe at different temperatures (Figure S16) was determined with help of Figure S1. The known concentration of free Xe at T = 293 K was used as reference and set to 2,340 μM[1]. At different temperatures, the peak areas for free Xe was put in relation to this. The experimental setup was as described previously[1].

References

[1] M. Kunth, C. Witte, and L. Schröder. Quantitative chemical exchange saturation transfer with hyperpolarized nuclei (qhyper-cest): Sensing xenon-host exchange dynamics and binding affinities by nmr. *J. Chem. Phys.*, 141(19):194202, 2014.

[2] Moritz Zaiss, Matthias Schnurr, and Peter Bachert. Analytical solution for the depolariza-

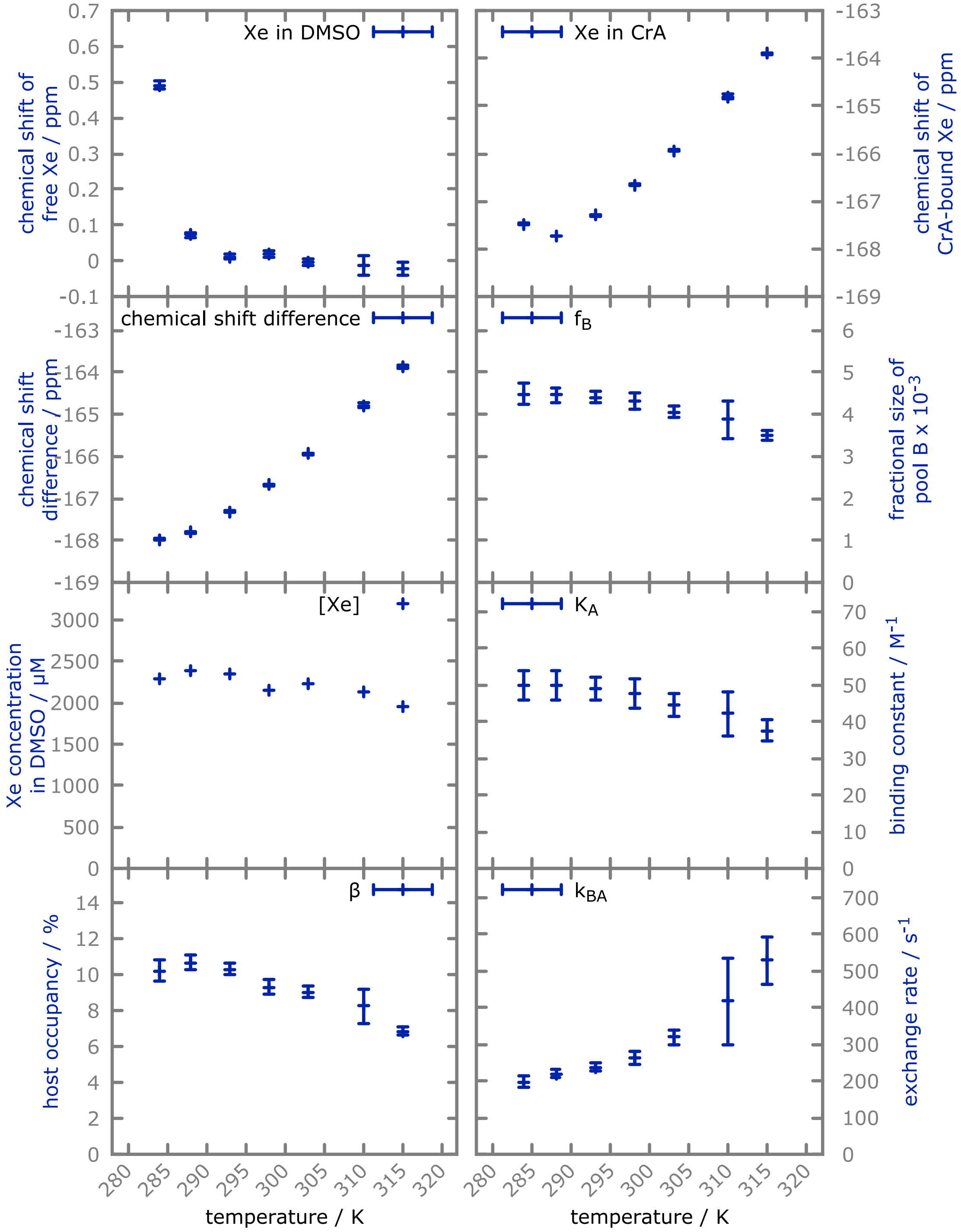

Figure S16: Xenon exchange kinetics at different temperatures studied by quantitative Hyper-CEST (sample: [CrA] = 100 μM in DMSO).

tion of hyperpolarized nuclei by chemical exchange saturation transfer between free and encapsulated xenon (hypercest). *J. Chem. Phys.*, 136(14):144106, 2012.

[3] Oscar Millet, J. Patrick Loria, Christopher D. Kroenke, Miquel Pons, and Arthur G. Palmer. The static magnetic field dependence of chemical exchange linebroadening defines the nmr chemical shift time scale. *J. Am. Chem. Soc.*, 122(12):2867–2877, 2000.

[4] Harden M. McConnell. Reaction rates by nuclear magnetic resonance. *J. Chem. Phys.*, 28(3):430–431, 1958.

[5] Kristin Bartik, Michel Luhmer, Jean-Pierre Dutasta, André Collet, and Jacques Reisse. ^{129}xe and ^{1}h nmr study of the reversible trapping of xenon by cryptophane-a in organic solution. *J. Am. Chem. Soc.*, 120(4):784–791, 1998.

[6] Sergey Korchak, Wolfgang Kilian, and Lorenz Mitschang. Degeneracy in cryptophane–xenon complex formation in aqueous solution. *Chem. Commun.*, 51:1721–1724, 2015.

[7] Martin Kunth, Christopher Witte, Andreas Hennig, and Leif Schröder. Identification, classification, and signal amplification capabilities of high-turnover gas binding hosts in ultrasensitive nmr. *Chem. Sci.*, 6:6069–6075, 2015.

[8] Martin Kunth, George J. Lu, Christopher Witte, Mikhail G. Shapiro, and Leif Schröder. Protein nanostructures produce self-adjusting hyperpolarized magnetic resonance imaging contrast through physical gas partitioning. *ACS Nano*, 12(11):10939–10948, 2018. PMID: 30204404.

[9] Martin Kunth, Christopher Witte, and Leif Schröder. Continuous-wave saturation considerations for efficient xenon depolarization. *NMR Biomed.*, 28(6):601–606, 2015.

[10] J.P Carver and R.E Richards. A general two-site solution for the chemical exchange produced dependence of t_2 upon the carr-purcell pulse separation. *J. Mag. Reson.*, 6(1):89 – 105, 1972.

[11] Andrew J. Baldwin. An exact solution for $r_{2,\text{eff}}$ in cpmg experiments in the case of two site chemical exchange. *J. Mag. Reson.*, 244:114 – 124, 2014.

[12] Hans Koss, Mark Rance, and Arthur G. Palmer. General expressions for carr–purcell–meiboom–gill relaxation dispersion for n-site chemical exchange. *Biochemistry*, 57(31):4753–4763, 2018. PMID: 30040382.

[13] S. Winkelmann, T. Schaeffter, T. Koehler, H. Eggers, and O. Doessel. An optimal radial profile order based on the golden ratio for time-resolved mri. *IEEE Trans. Med. Imag.*, 26(1):68–76, 2007.

[14] Philipp Ehses, Nicole Seiberlich, Dan Ma, Felix A. Breuer, Peter M. Jakob, Mark A. Griswold, and Vikas Gulani. Ir truefisp with a golden-ratio-based radial readout: Fast quantification of t_1, t_2, and proton density. *Magn. Reson. Med.*, 69(1):71–81, 2013.

[15] M. Kunth, N. Seiberlich, P. Ehses, V. Gulani, and M.A. Griswold. Improvement of quantitative mri using radial grappa in conjunction with ir-truefisp. *ISMRM - Stockholm*, page 2895, 2010.

[16] Petri Peuravaara, Jouni Karjalainen, Jianfeng Zhu, Jiří Mareš, Perttu Lantto, and Juha Vaara. Chemical shift extremum of ^{129}xe(aq) reveals details of hydrophobic solvation. *Sci. Rep.*, 8:7023, 2018.

[17] H. Lawrence Clever. *Krypton, Xenon and Radon – Gas Solubilities*. Pergamon, Oxford, Chemistry Department, Emory University, Atlanta, GA, USA, 2 edition, 1979.